Non-constant link tension coefficient in the tumbling-snake model subjected to simple shear

Pavlos S. Stephanou (iD), and Martin Kröger (iD)

View Online   **Export Citation**   **CrossMark**

Non-constant link tension coefficient in the tumbling-snake model subjected to simple shear

Pavlos S. Stephanou[1] and Martin Kröger[2]

[1]*Department of Mathematics and Statistics, University of Cyprus, P.O. Box 20537, 1678 Nicosia, Cyprus*
[2]*Department of Materials, Polymer Physics, ETH Zürich, CH-8093 Zürich, Switzerland*

The authors of the present study have recently presented evidence that the tumbling-snake model for polymeric systems has the necessary capacity to predict the appearance of pronounced undershoots in the time-dependent shear viscosity as well as an absence of equally pronounced undershoots in the transient two normal stress coefficients. The undershoots were found to appear due to the tumbling behavior of the director **u** when a rotational Brownian diffusion term is considered within the equation of motion of polymer segments, and a theoretical basis concerning the use of a link tension coefficient given through the nematic order parameter had been provided. The current work elaborates on the quantitative predictions of the tumbling-snake model to demonstrate its capacity to predict undershoots in the time-dependent shear viscosity. These predictions are shown to compare favorably with experimental rheological data for both polymer melts and solutions, help us to clarify the microscopic origin of the observed phenomena, and demonstrate in detail why a constant link tension coefficient has to be abandoned. *Published by AIP Publishing.* https://doi.org/10.1063/1.4991935

I. INTRODUCTION

Since its introduction, back in the 1970s, the tube model of de Gennes and Doi-Edwards (DE)[1–3] has been proven able to enhance our understanding of the dynamical behavior of high molecular weight (MW) entangled polymer melts and concentrated polymer solutions, both under equilibrium and flow conditions.[4,5] Its notions, like those of the confining mean-field tube and the primitive path (PP), have today been obtained from lower-level simulations. These simulations have provided the means to study the entanglement statistics[6–9] and to follow the dynamics of the PP network,[10–13] leading eventually to the reevaluation of modern tube models[14–16] and allowing for multi-scale modeling approaches to emerge.[17–20]

An extended single-segment kinetic theory model, later coined the tumbling-snake model,[21] has been obtained by Curtiss and Bird (CB) by following a completely different approach and without making the same assumptions as those made by DE.[22–27] Yet, the tube/reptation formulation is a special case of the tumbling-snake model when two of its parameters, (i) the link tension coefficient (ε), which arises from the anisotropy of the friction tensor, and (ii) the dimensionless orientational diffusion coefficient of polymer segments (ε'), are both set to zero. Up until recently, the tumbling-snake model had only been solved for an analytically tractable case, i.e., in the absence of rotational diffusion, $\varepsilon' = 0$. We recently filled this void by solving the full tumbling-snake model in the case of simple shear flow.[21,27] We further suggested that it bears the necessary characteristics to quantitatively compare against high-shear-rate startup experimental data that reveal an undershoot, right after the overshoot, in the transient shear viscosity.[21] The appearance of the undershoot, as first proposed by Costanzo *et al.*,[28] had been associated to the

tumbling of polymer chains.[29,30] Along these lines, it was conjectured to be more pronounced in concentrated polymer solutions than in entangled polymer melts[21,28] despite the fact that undershoots have been noted in polymer melts as well.[31] Via rheological measurements of a polystyrene solution, we had shown[21] that such a behavior is absent (within statistical uncertainty) in the two normal stress coefficients. Furthermore, we illustrated that the tumbling-snake model is able to capture the observed behavior qualitatively only (i) for non-vanishing orientational diffusion and (ii) if complemented by a link tension coefficient related to the nematic order parameter S_2.[32] It is worthwhile mentioning that there exist simulation results and complementary theoretical evidence for the appearance of such undershoots, namely, the single-segment models of Graham, Likhtman, Milner, and McLeish (GLaMM),[33] the thermodynamically admissible reptation model of Fang *et al.*,[34] as well as slip-link simulations by Schieber *et al.*[35]

In the present work, we provide a more thorough parametrization of the tumbling-snake model compared with previous work.[21] The structure of the paper is as follows: Sec. II introduces the model. In Sec. III, we provide the expansion of the material functions with respect to the dimensionless shear rate and time. In Sec. IV, we solve the tumbling-snake model numerically using Brownian dynamics (BD) simulations and proceed in Sec. V to compare its predictions with the experimental data of Costanzo *et al.*[28] The paper concludes with Sec. VI where we discuss the significance of our work and elaborate on future research endeavors.

II. MODEL

Within the tumbling-snake model, each polymer chain is primarily modeled as a Kramers freely jointed bead-rod chain with N beads linearly connected by $N − 1$ rods each of fixed

length a,[22–26] subjected to flow. The evolution equation for the single-link distribution function $f(\sigma, \mathbf{u}, t)$, also denoted as Fokker-Planck (FP) equation, describes the probability to find a tangent unit vector $\mathbf{u}$ at time t at the relative polymer contour position $\sigma \in [0, 1]$. It is given by[27]

$$\frac{\partial f}{\partial t} = \frac{1 - \varepsilon'}{\lambda} \frac{\partial^2 f}{\partial \sigma^2} + \frac{\varepsilon'_0}{\lambda} \frac{\partial}{\partial \mathbf{u}} \cdot \frac{\partial f}{\partial \mathbf{u}} - \frac{\partial}{\partial \mathbf{u}} \cdot (\mathbf{\Gamma} f), \quad (1)$$

where $\varepsilon' = \varepsilon'_0 (N - 1)^{-2}$ characterizes the orientational diffusivity relative to one-dimensional curvilinear diffusion along the polymer contour, $\mathbf{\Gamma} = (\boldsymbol{\delta} - \mathbf{uu}) \cdot \boldsymbol{\kappa} \cdot \mathbf{u}$ is a torque associated with flow, where $\boldsymbol{\kappa}$ denotes the transposed velocity gradient tensor and $\boldsymbol{\delta}$ is the unit tensor, $\lambda = \zeta a^2 (N - 1)^2 N^{1+\beta} / 2k_B T$ is the characteristic time of the chain related to the reptation time τ_d introduced by DE via $\lambda = \pi^2 \tau_d$, where ζ is the bead friction coefficient and β is the chain constraint exponent.[22–26] By requiring that the stress tensor expression of the tumbling-snake model with $\varepsilon' = \varepsilon = 0$ matches the DE model,[23,36] the number of beads per chain can be related to the number of chain entanglements, Z, employed by DE via the relation $N = 3Z$. Note that Eq. (1) is slightly more general than Eq. (19.3-26) in Ref. 26 as it does not assume $N \gg 1$. The first term on the right hand-side of Eq. (1) is the reptation term describing curvilinear segment diffusion along the polymer's contour. When $\varepsilon' = 0$ the segments strictly reptate along their own chain contour, whereas for $\varepsilon' > 0$ segments are also allowed to explore the surrounding space. The second term describes orientational diffusion, capturing the constraint release (CR) mechanism. It is controlled by the parameter $\varepsilon'_0 \in [0, 1]$.[27,36] The third term represents the deterministic effect of the applied homogeneous flow field. The single-link distribution function is normalized to unity, $\int_0^1 \int f(\sigma, \mathbf{u}, t) d\mathbf{u} d\sigma = 1$, for all t. Chain ends are always oriented at random,

$$\forall_t \quad f(0, \mathbf{u}, t) = f(1, \mathbf{u}, t) = \frac{1}{4\pi}. \quad (2)$$

This assumption is done here in accord with both CB and DE[21,27] while it can be expected to fail under flow conditions in which case chain ends experience the anisotropy of the surrounding matrix.[32,37] The tumbling-snake model reduces to the DE model for $\varepsilon' = 0$, while for $\varepsilon' = 1$, it coincides with the orientational diffusion equation for rigid dumbbells, rods, ellipsoids, or multibead rods.[22–27] It should be noted that only the model with $\varepsilon' = 0$ bears an analytical solution.[22–26] The tumbling-snake model with $\varepsilon' > 0$ can be solved via the use of Brownian dynamics (BD).[21,27]

The (extra or polymeric) stress tensor $\boldsymbol{\tau}$ of the tumbling-snake model for an incompressible, monodisperse polymer melt at monomer number density n is given by[26,27]

$$\begin{aligned} \frac{\boldsymbol{\tau}(t)}{G} = & -(1 - \varepsilon') \left(\langle \mathbf{uu} \rangle^{(1)}(t) - \frac{1}{3} \boldsymbol{\delta} \right) \\ & - 3\varepsilon'_0 \left(\langle \mathbf{uu} \rangle^{(2)}(t) - \frac{1}{18} \boldsymbol{\delta} \right) \\ & - \varepsilon \mathbf{B}(t), \end{aligned} \quad (3)$$

with modulus $G = nk_B T(N - 1)$. The stress tensor involves the following orientational averages calculated with the time-dependent single-link orientational probability distribution function $f(\sigma, \mathbf{u}, t)$,

$$\langle \mathbf{uu} \rangle^{(1)}(t) = \int_0^1 d\sigma \int d\mathbf{u} f(\sigma, \mathbf{u}, t) \mathbf{uu},$$

$$\langle \mathbf{uu} \rangle^{(2)}(t) = \int_0^1 \sigma(1 - \sigma) d\sigma \int d\mathbf{u} f(\sigma, \mathbf{u}, t) \mathbf{uu}, \quad (4)$$

$$\mathbf{B}(t) = \tilde{\boldsymbol{\kappa}} : \int_0^1 \sigma(1 - \sigma) d\sigma \int d\mathbf{u} f(\sigma, \mathbf{u}, t) \mathbf{uuuu},$$

with $\tilde{\boldsymbol{\kappa}} \equiv \lambda \boldsymbol{\kappa}$. During BD, these moments are evaluated as ensemble averages, and a calculation of f is not required to evaluate the stress tensor. In Eq. (3), ε is the link tension coefficient that controls the anisotropy of the friction tensor within the kinetic theory derivation of CB.[22–26] In the original treatment, ε was considered to be a constant coefficient. It is this assumption which rendered the model apparently unrealistic: it leads to a violation of the stress-optic law (expected to hold close to equilibrium), the transient, both shear and elongational, viscosities approach a finite value in the limit $t \to 0$, and the transient second normal stress coefficient exhibits spurious sign changes with time before eventually becoming negative under steady-state conditions (see also Figs. S1 and S4 of the supplementary material). To remedy these inconsistencies, we proposed in Ref. 21 to employ a time- and shear-rate-dependent link tension coefficient given as $\varepsilon = \varepsilon_0 S_2^2$, where ε_0 is a constant coefficient characterizing the material and $S_2 \in [0, 1]$ is the uniaxial order parameter,

$$S_2^2 = \frac{3}{2} \text{tr}(\langle \mathbf{uu} \rangle_{\text{ani}} \cdot \langle \mathbf{uu} \rangle_{\text{ani}}), \quad (5)$$

calculated from the anisotropic orientation tensor $\langle \mathbf{uu} \rangle_{\text{ani}} \equiv \langle \mathbf{uu} \rangle^{(1)} - \frac{1}{3} \boldsymbol{\delta}$, that vanishes at equilibrium and approaches unity in a totally aligned state. For the case of incompressible shear flow, $\tilde{\boldsymbol{\kappa}}$ is traceless and contains the dimensionless flow strength, the Weissenberg number, $\text{Wi} \equiv \dot{\gamma} \lambda$, on one of its non-diagonals.

The model can be solved numerically, and its stress tensor evaluated for both steady and time-dependent incompressible flows, via Brownian dynamics as described elsewhere.[21,27] The numerical results are validated against exact analytical solutions available for weak flows, to be summarized next. Since BD noise is especially disturbing at low rates and small times, the analytical results can also be used in these regimes. In two limiting cases, the tumbling-snake model must reduce to known results for rigid rods and the original tube model.

III. SMALL SHEAR RATE EXPANSION

A. Steady-state predictions

We begin by considering a steady-state spherical harmonics expansion of the single-link distribution function around equilibrium under steady-state shear. To this end, we can merely overtake the strategy presented in Ref. 27 while newly accounting for a link tension coefficient $\varepsilon = \varepsilon_0 S_2^2$ with S_2 given by Eq. (5).

Up to second order in Wi, we obtain

$$\varepsilon = \varepsilon_0 \frac{4}{75} (\Gamma_1 \text{Wi})^2, \qquad (6)$$

where Γ_1 is defined in Eq. (A1b) of the supplementary material. The link tension coefficient is thus expected to vanish in the absence of shear. The corresponding shear viscosity η and viscometric functions are given as

$$\frac{\eta}{G\lambda} = \frac{1}{60} - \frac{2}{245}\left(4\Delta_3 + \frac{23}{3}\Delta_2\right)\text{Wi}^2 + \frac{2\varepsilon_0}{3375}(\Gamma_1\text{Wi})^2,$$

$$\frac{\Psi_1}{G\lambda^2} = \frac{2\Delta_1}{15} - \frac{4}{63}\left(\Delta_5 + \frac{3}{35}\Delta_4\right)\text{Wi}^2, \qquad (7)$$

$$\frac{-\Psi_2}{G\lambda^2} = \frac{4\Delta_1}{105} - 2\left(\frac{4\Delta_4}{5145} + \frac{\Delta_5}{63} - \frac{\Delta_6}{3773}\right)\text{Wi}^2,$$

where the coefficients Δ_i, $i = 2, .., 6$, are defined in Eq. (A1b) of the supplementary material. It is readily seen that the analytical results for the viscometric functions Ψ_1 and Ψ_2, at least up to second order terms, are identical to the predictions when $\varepsilon = 0$, cf. Eq. (6) in Ref. 27. The use of a variable link tension coefficient $\sim S_2^2$ thus implies that $-\Psi_{2,0}/\Psi_{1,0} = 2/7$ irrespective of ε' and ε_0.

B. Transient predictions

Next, we consider a time-dependent spherical harmonics expansion of the single-link distribution function around equilibrium to be able to obtain the linear viscoelastic (LVE) analytical predictions. The methodology employed is described in Sec. C of the supplementary material of Ref. 21, and the final expression for the expansion, up to 2nd order in Wi, is given in their Eq. (A8). Upon inserting the expansion into Eqs. (4) and by furthermore inserting $\varepsilon = \varepsilon_0 S_2^2$ into the stress tensor expression Eq. (3), one obtains the LVE expansion of the material functions. The final result, first presented in Ref. 21, reads (see Sec. A2 of the supplementary material)

$$\frac{\eta(t)}{G\lambda} = \frac{\eta_0}{G\lambda} - \frac{1}{15}\Delta_0(t),$$

$$\frac{\Psi_1(t)}{G\lambda^2} = \frac{\Psi_{1,0}}{G\lambda^2} - \frac{2}{15}\left(\Delta_1(t) + \frac{t}{\lambda}\Delta_0(t)\right), \qquad (8)$$

$$\frac{\Psi_2(t)}{G\lambda^2} = \frac{\Psi_{2,0}}{G\lambda^2} + \frac{4}{105}\left(\Delta_1(t) + \frac{t}{\lambda}\Delta_0(t)\right),$$

FIG. 1. Predictions for the link tension coefficient, $\varepsilon/\varepsilon_0$, as a function of dimensionless shear rate Wi for $N = 100$ ($Z \approx 33$) and various values of ε_0'. The thick lines give the predictions of Eq. (6) when $\varepsilon_0' = 0$ (dark blue) and 0.9 (dark yellow).

where η_0, $\Psi_{1,0}$, and $\Psi_{2,0}$ are the corresponding zero-rate quantities of the material functions given by Eq. (7) with Wi = 0, and $\Delta_i(t)$ are defined in Eq. (A3b) of the supplementary material.

It is insightful to verify that the above expressions correctly capture the rigid rod case. By taking the limit $\varepsilon' = 1$ and $N = 2$ with $G = 6G_{\text{rd}}$ and $\lambda = 6\lambda_{\text{rd}}$ in Eq. (A4a) of the supplementary material, we obtain

$$\frac{\eta(t)}{G_{\text{rd}}\lambda_{\text{rd}}} = \frac{\eta_0}{G_{\text{rd}}\lambda_{\text{rd}}} - \frac{3}{5}\exp(-t/\lambda_{\text{rd}}),$$

$$\frac{\Psi_1(t)}{G_{\text{rd}}\lambda_{\text{rd}}^2} = \frac{\Psi_{1,0}}{G_{\text{rd}}\lambda_{\text{rd}}^2} - \frac{6}{5}\left(1 + \frac{t}{\lambda_{\text{rd}}}\right)\exp(-t/\lambda_{\text{rd}}), \qquad (9)$$

$$\frac{\Psi_2(t)}{G_{\text{rd}}\lambda_{\text{rd}}^2} = \frac{\Psi_{2,0}}{G_{\text{rd}}\lambda_{\text{rd}}^2} + \frac{12}{35}\left(1 - \varepsilon + \frac{t}{\lambda_{\text{rd}}}\right)\exp(-t/\lambda_{\text{rd}}),$$

where η_0, $\Psi_{1,0}$, and $\Psi_{2,0}$ are the corresponding zero-rate quantities of the material functions for the rigid rod, cf. Eq. (11) of Ref. 27 for $\text{Wi}_{\text{rd}} \equiv \dot{\gamma}\lambda_{\text{rd}} = 0$,

$$\frac{\eta_0}{G_{\text{rd}}\lambda_{\text{rd}}} = \frac{3}{5}\left(1 + \frac{2}{3}\varepsilon\right),$$

$$\frac{\Psi_{1,0}}{G_{\text{rd}}\lambda_{\text{rd}}^2} = \frac{6}{5}, \qquad (10)$$

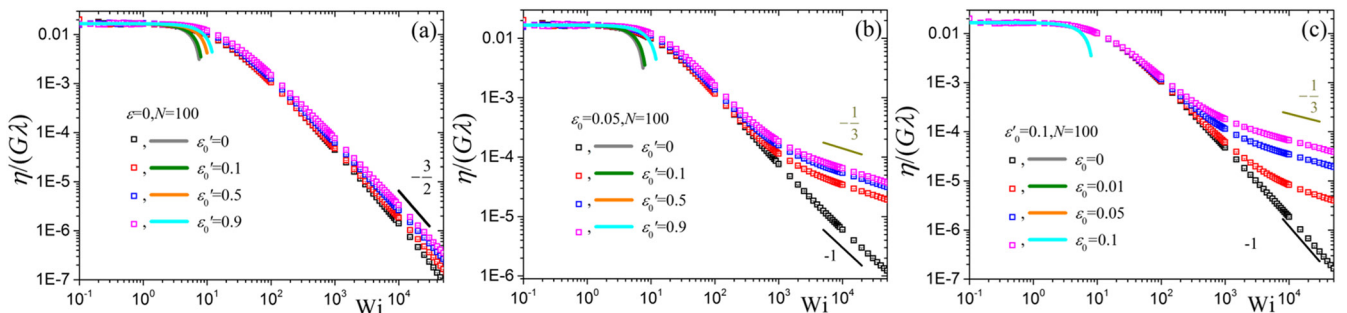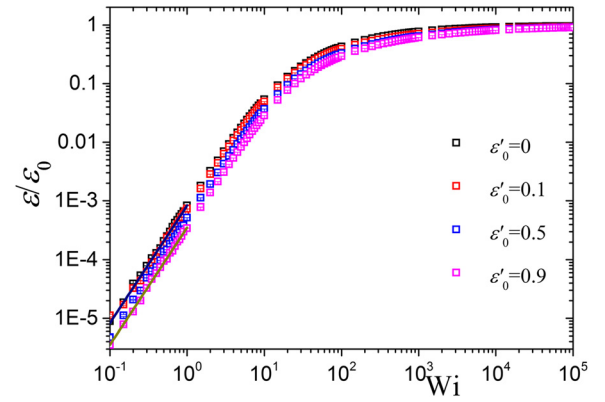$$\frac{\Psi_{2,0}}{G_{\text{rd}}\lambda_{\text{rd}}^2} = -\frac{12(1-\varepsilon)}{35}.$$

FIG. 2. Predictions for the shear viscosity η as a function of dimensionless shear rate Wi for $N = 100$ ($Z \approx 33$) and various values of ε_0' and ε_0. The thick lines give the predictions of Eq. (7), whereas the straight lines depict power laws at large Wi.

FIG. 3. Predictions for the first viscometric function Ψ_1 as a function of dimensionless shear rate Wi for $N = 100$ ($Z \approx 33$) and various values of ε'_0 and ε_0. The thick lines give the predictions of Eq. (7), whereas the straight lines depict power laws at large Wi.
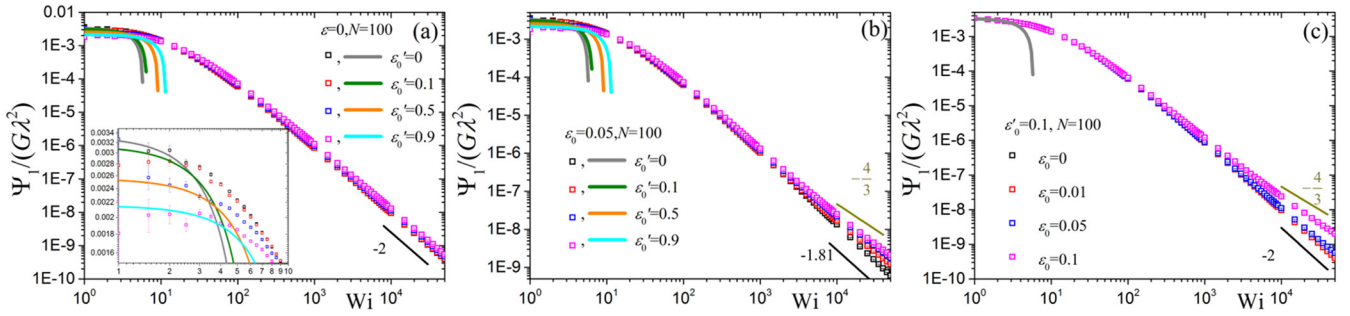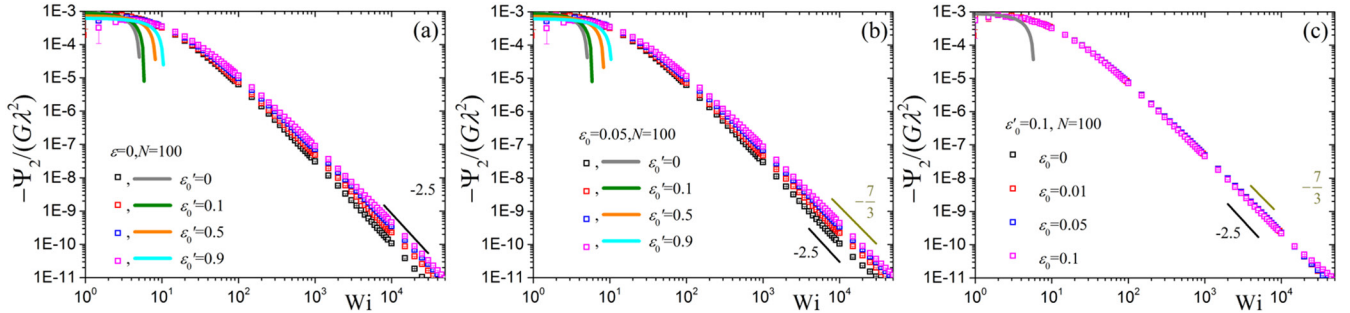

FIG. 4. Predictions for the second viscometric function Ψ_2 as a function of dimensionless shear rate Wi for $N = 100$ ($Z \approx 33$) and various values of ε'_0 and ε_0. The thick lines give the predictions of Eq. (7), whereas the straight lines depict power laws at large Wi.

The time-dependent expressions for the material functions during start-up of shear flow, Eq. (10), are identical with those that can be obtained for the rigid rod when $\varepsilon = 1$. To see this, one has to identify $\varepsilon = \lambda_2^{(2)}/\lambda_2^{(1)}$ in Eqs. (11.8)–(11.10) of Ref. 38.

IV. COMPLETE SOLUTION USING BROWNIAN DYNAMICS SIMULATIONS

A. Steady-state behavior

We first present a parametrization of the steady-state predictions of the tumbling-snake model with time-dependent and shear rate-dependent coefficient $\varepsilon = \varepsilon_0 S_2^2$. Figure 1 shows the squared order parameter, or reduced link tension coefficient, $\varepsilon/\varepsilon_0$, as a function of the dimensionless shear rate Wi along with the analytical results for small Wi given by Eq. (6). As can be seen, the link tension coefficient varies quadratically with Wi at small shear rates, in accord with Eq. (6), and the order parameter seems to approach unity at large shear rates, independently of the value of ε'_0.

The steady-state shear viscosity as a function of the dimensionless shear rate Wi is depicted in Fig. 2 along with the analytical results for small Wi according to Eq. (7). As expected, the zero-shear rate limit is seen to be independent of ε_0 and equals $G\lambda/60$, whereas employing a constant link tension coefficient as suggested within the original CB treatment, the same limit is known as $G\lambda(1 + \frac{2}{3}\varepsilon)/60$.[26,27] At large shear rates, the slopes of $\ln \eta$ with respect to $\ln$ Wi are the same as those (Fig. 1 in Ref. 27) we had measured when ε remains a constant: when $\varepsilon_0 > 0$, the slope is seen to be decreasing from the value of -1, for the non-tumbling model ($\varepsilon' = 0$), to $-1/3$

when ε'_0 approaches unity (see also Fig. 4 in Ref. 27). The simple underlying reason is the order parameter that saturates at large shear rate at a high value close to unity, implying $\varepsilon \approx \varepsilon_0$ (see Fig. 1).

The steady-state first and second normal stress coefficients as a function of Wi are presented in Figs. 3 and 4, respectively. Again, in agreement with Eq. (7), the zero-shear-rate limit of both coefficients is seen to be independent of ε_0. Actually, for the first normal stress coefficient, we obtain the same zero-shear rate limit as that obtained assuming a strictly constant link tension coefficient [see also Eq. (6) in Ref. 27]. On the other hand, the prediction for the second normal stress is now seen to be independent of ε_0. The power laws at high shear
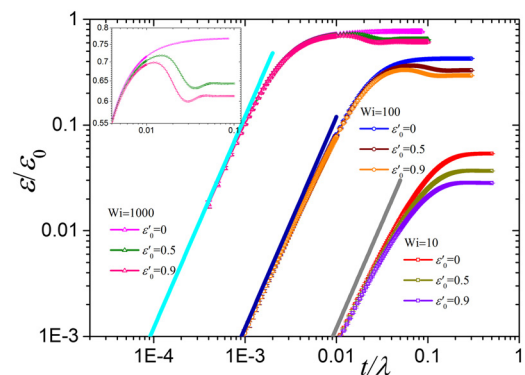

FIG. 5. Predictions for the link tension coefficient, $\varepsilon/\varepsilon_0$, as a function of dimensionless time for $N = 100$ ($Z \approx 33$) and various values of the parameter ε'_0 and dimensionless shear rates Wi. The thick lines give the predictions of $\frac{9}{75}(\dot{\gamma}t)^2$.
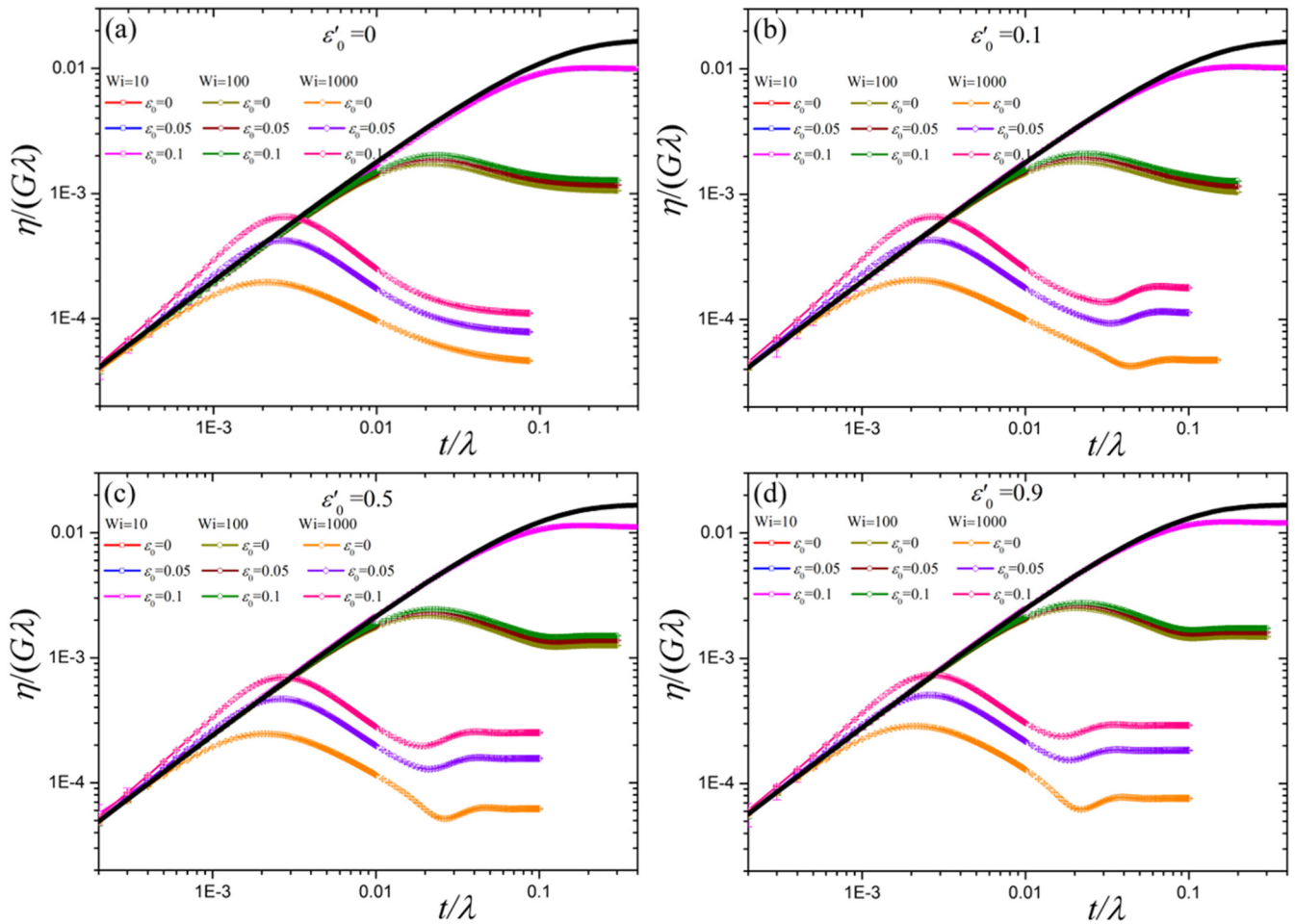
FIG. 6. Predictions for the transient shear growth viscosity $\eta(t)$ as a function of time for $N = 100$ ($Z \approx 33$) and various values of the parameter ε_0 and dimensionless shear rate Wi for (a) $\varepsilon'_0 = 0$, (b) $\varepsilon'_0 = 0.1$, (c) $\varepsilon'_0 = 0.5$, and (d) $\varepsilon'_0 = 0.9$. The thick lines give the predictions of Eq. (8).

rates are, similar to those for the shear viscosity, the same as those obtained when a constant link tension coefficient is employed (see Fig. 4 in Ref. 27).

B. Transient behavior

Figure 5 shows the link tension coefficient, $\varepsilon/\varepsilon_0$, as a function of the dimensionless time t/λ for various values of the shear rate Wi and ε'_0 along with the analytical results for small times, provided in Eq. (A5) of the supplementary material. It varies quadratically with $\dot{\gamma}t$ at small times; when Wi = 10, we find a monotonic approach toward the steady-state value,

which is seen to decrease with ε'_0, in agreement with the shift of the steady-state curve to larger shear rates by increasing ε'_0 (Fig. 1). At larger shear rates, a damping behavior is seen in the approach to the steady-state when $\varepsilon'_0 > 0$, which is particularly obvious when Wi = 1000 (see inset).

Figure 6 shows the transient viscosity $\eta(t)$ as a function of the dimensionless time for various dimensionless shear rates along with the LVE prediction, cf. Eq. (8). The LVE prediction captures the time behavior of all material functions shown in Figs. 6, 9, and 10 for Wi $\lesssim$ 1. For all shear rates, the viscosity vanishes at $t = 0$ irrespective of the value of the parameters ε'_0 and ε_0. This numerical finding is consistent with
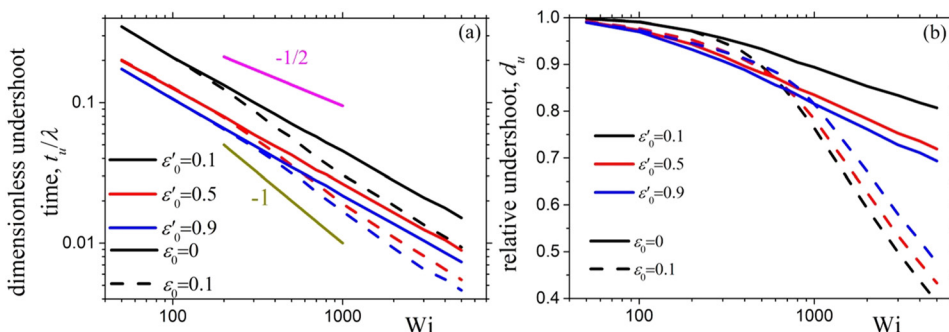

FIG. 7. Predictions for (a) the dimensionless undershoot time, t_u/λ, and (b) the relative undershoot depth (undershoot value divided by steady-state value), d_u, for various values of ε'_0 and ε_0 as a function of the dimensionless shear rate Wi. Slopes of -1 and $-1/2$ are depicted in (a).
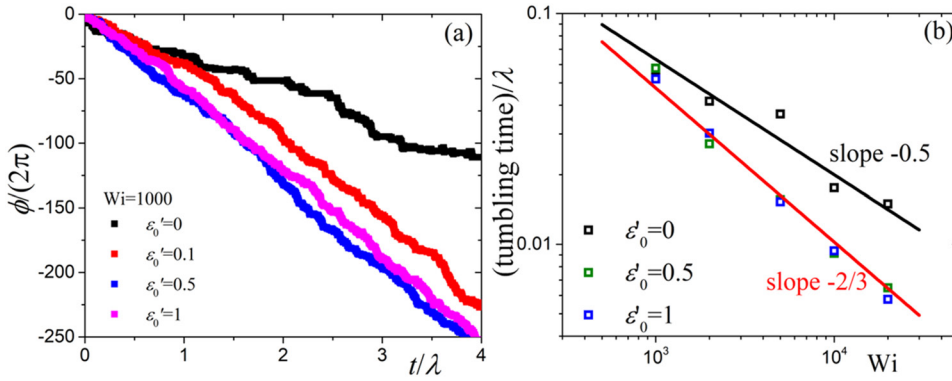
FIG. 8. Predictions for (a) the time course of the orientational angle of the polymer chain end-to-end vector, $\phi/(2\pi)$, when Wi = 1000, and (b) the dimensionless tumbling time, given as the absolute inverse slope of $\phi/(2\pi)$ with time, as a function of the dimensionless shear rate Wi, for various values of ε_0'. Lines are guide to the eye and depict slopes of $-1/2$ and $-2/3$.

the analytical Eq. (8) because $\Delta_0(0) = 24 \sum_{\nu=1,3,\ldots}^{\infty} (\nu\pi)^{-4} = 1/4$ [see Eq. (A4b) of the supplementary material]. At the same time, it is the behavior supported by experiments.[21,28,31] In contrast, the model with a constant link tension coefficient predicts that as $t \to 0$ the reduced shear viscosity approaches the constant value $\varepsilon/90$ irrespective of the value of the parameter ε_0' (see Fig. S1 of the supplementary material). This unappealing feature of the original model was already recognized by Bird *et al.* in their studies.[24] Irrespective of the shear rate imposed and the values of the parameters ε_0' and ε_0, the growth of the

viscosity strictly follows the LVE prediction, Eq. (8), at small times. Focusing on the smallest shear rates (Wi $\leq$ 10), the viscosity monotonically reaches the steady-state value at large times irrespective of the parameters ε_0' and ε_0. The steady-state value is seen to be independent of ε_0' and ε_0, in agreement with Fig. 2. As we increase the shear rate further up to Wi = 100, the shear viscosity reaches an overshoot before visually approaching the steady-state value from above; note that the predictions for $\varepsilon_0' = 0$ and 0.1 are almost indistinguishable. The overshoot shifts upwards upon increasing ε_0', but as ε_0 is increased, this
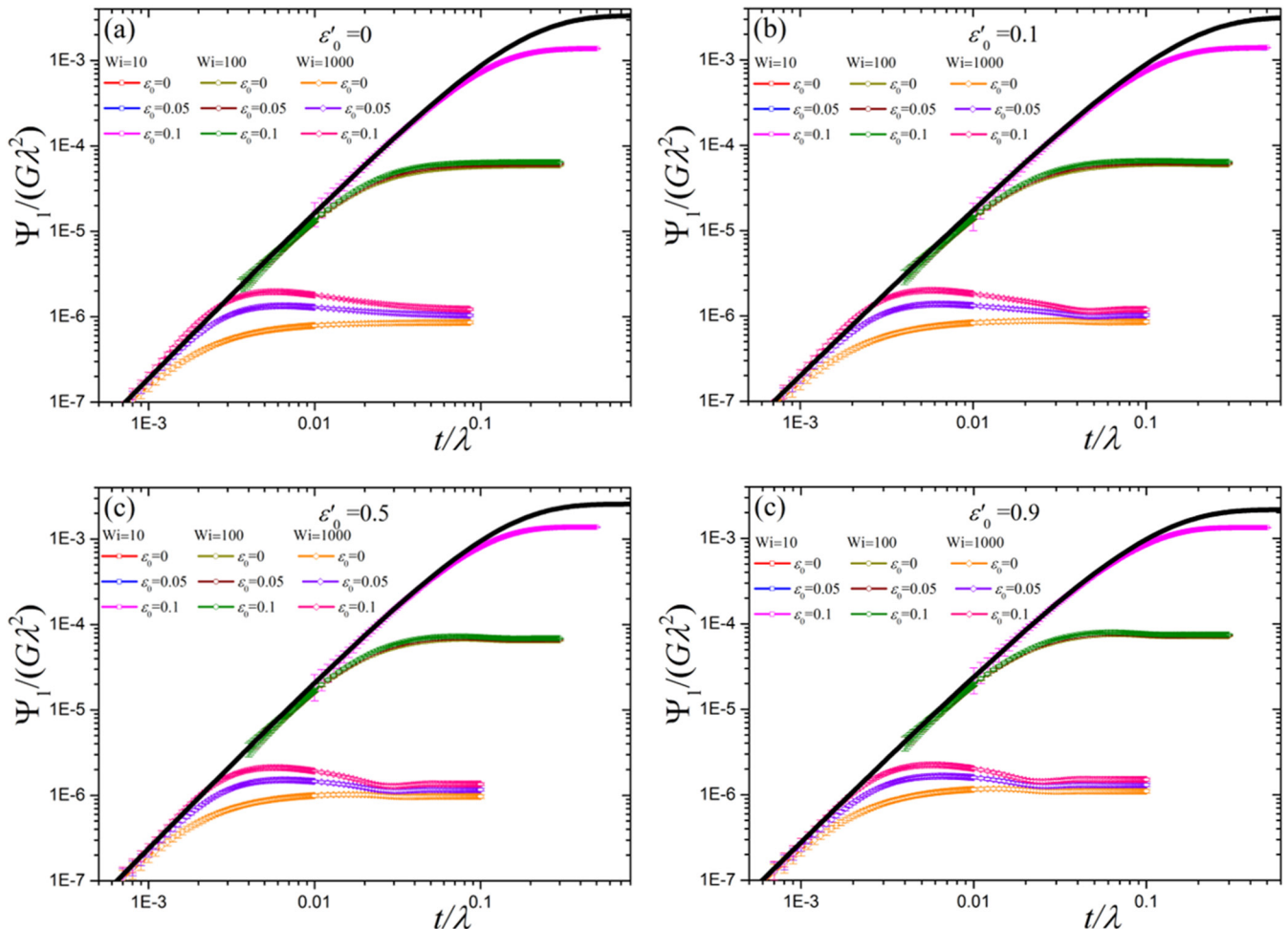

FIG. 9. Predictions for the shear growth first normal stress coefficient as a function of time for $N = 100$ ($Z \approx 33$) and various values of the parameter ε_0 and dimensionless shear rate Wi for (a) $\varepsilon_0' = 0$, (b) $\varepsilon_0' = 0.1$, (c) $\varepsilon_0' = 0.5$, and (d) $\varepsilon_0' = 0.9$. The thick lines give the predictions of Eq. (8).

difference becomes smaller. By increasing the dimensionless shear rate to Wi = 1000, an undershoot is clearly observed for $\varepsilon_0' > 0$ following the overshoot; actually, a tiny undershoot is also measurable when Wi = 100, as we will illustrate later. It is worthwhile noting in Fig. 6(a) that the non-tumbling model ($\varepsilon_0' = 0$) completely fails to predict such a damping behavior since, following the overshoot, curves approach the steady-state value monotonically from above, as first mentioned in Ref. 21.

To better quantify the impact of the two parameters, ε_0 and ε_0', on the position and depth of the undershoot in $\eta(t)$, we extract and plot the dimensionless time t_u/λ at which the undershoot occurs in Fig. 7(a), and the relative undershoot depth, d_u, as a function of the dimensionless shear rate in Fig. 7(b). Subjected to constant ε_0 and shear rate, the undershoot position shifts toward smaller times when ε_0' is increased. At constant ε_0', the undershoot position is seen to be independent of ε_0 at small shear rates, but it shifts to smaller times at shear rates Wi $\gtrsim$ 200. When $\varepsilon = 0$ the shift to smaller times seems to follow a power law behavior with an exponent of about −0.67 and is seen to be quite insensitive to ε_0'. On the other hand, when $\varepsilon_0 > 0$, the exponent seems to be decreasing to a value of about −0.8 and remains approximately independent of ε_0'. The relative undershoot depth, d_u, approaches unity upon decreasing Wi irrespective of the chosen ε_0' and ε_0 values

[Fig. 7(b)]. For the case of constant $\varepsilon_0' > 0$, d_u with $\varepsilon_0 = 0.1$ reside above the corresponding results for $\varepsilon_0 = 0$ initially (i.e., exhibiting a shallower undershoot), but at larger shear rates, the prediction for $\varepsilon_0 = 0.1$ decreases much more steeply (in concert with a deeper undershoot). On the other hand, at constant ε_0, d_u is again seen to decrease upon increasing ε_0'. The corresponding predictions for t_u/λ and d_u in the case of a constant ε_0 are provided in Fig. S2 of the supplementary material. They seem to share their qualitative behavior with the results shown in Fig. 7.

A more thorough investigation of the undershoot underpinnings can be undertaken by monitoring the time course of the unbound orientation angle ϕ of the polymer chain end-to-end vector in the shearing plane and the number of completed tumblings $\phi/2\pi$,[39] illustrated in Fig. 8(a). Upon increasing the value of ε_0', the slope of the $\phi(t)$ curve increases. Since this slope can be identified as the tumbling time,[40] tumbling intensifies with increasing ε_0'. While the FP equation contains a rotational drift term, the fully aligned segment does not experience any torsion in the absence of Brownian motion.[21,27] Thus at first glance, surprisingly, tumbling does occur even in the absence of rotational diffusion, i.e., for $\varepsilon_0' = 0$. This feature can be traced back to the boundary condition, Eq. (2), and the corresponding randomization of link orientations once a link has reached either chain end (within BD). This allows,
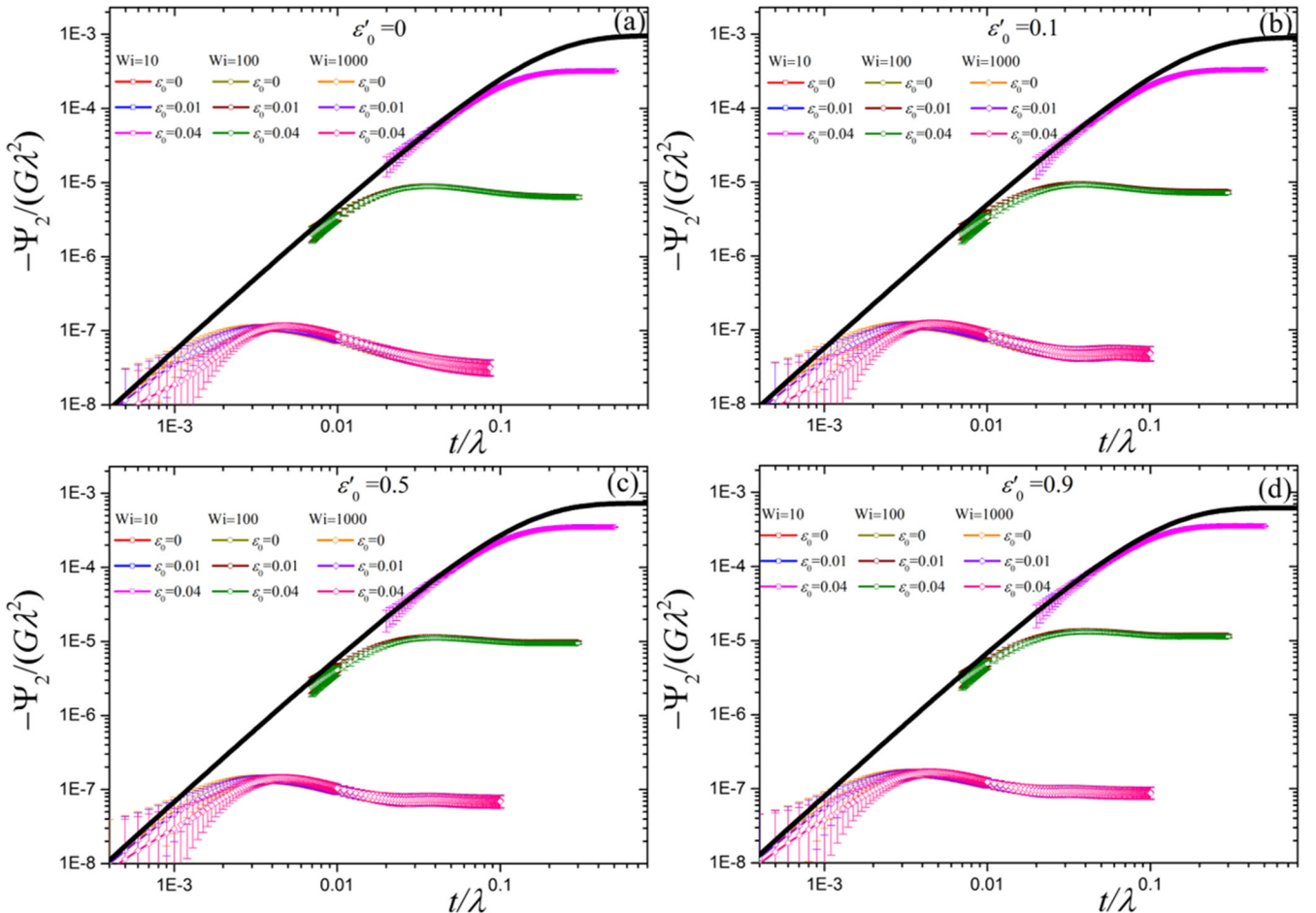

FIG. 10. Predictions for the shear growth second normal stress coefficient as a function of time for $N = 100$ ($Z \approx 33$) and various values of the parameter ε and dimensionless shear rate Wi for (a) $\varepsilon_0' = 0$, (b) $\varepsilon_0' = 0.1$, (c) $\varepsilon_0' = 0.5$, and (d) $\varepsilon_0' = 0.9$. The thick lines give the predictions of Eq. (8).

over time, for the chain to leave a fully aligned metastable state and to tumble. For comparison, we recall that a single non-Brownian infinitely thin rod would not tumble if the rotational component of the FP equation for the orientational distribution function was omitted. By plotting the tumbling time as a function of Wi [Fig. 8(b)], we do note that when $\varepsilon'_0 = 0$ the tumbling time decreases with the square root of Wi, whereas for $\varepsilon'_0 = 0.5$ and $\varepsilon'_0 = 1$, it decreases as $\dot{\gamma}^{-2/3}$, exactly coinciding with the theoretical scaling for a single Brownian rod.[39]

Figure 9 shows the transient first viscometric function versus dimensionless time for various dimensionless shear rates along with the LVE prediction, Eq. (8). The analytical expression for the LVE envelope allows us to disregard the simulation results for small times which come with large statistical uncertainties for both normal stresses. For this reason, all data at small times are not shown in Figs. 9 and 10 and Figs. S3 and S4 of the supplementary material. At the smallest shear rates (Wi = 10), the first viscometric function Ψ_1 monotonically approaches its steady-state value at large times irrespective of the parameters ε'_0 and ε_0. The predictions are seen to be practically independent of the value of ε'_0 and ε_0 (see also Fig. 3). The same is true when Wi = 100. For the largest

rate investigated, Wi = 1000, we do note that for any finite $\varepsilon'_0 > 0$, the overshoot is followed by a modest undershoot. The depth of the undershoot slightly increases with increasing ε_0 but is generally seen to be considerably less pronounced compared with the one the model yields for the transient shear viscosity (Fig. 6). The corresponding predictions under a constant ε are presented in Fig. S3 of the supplementary material. The main difference between the two sets is as follows: at large shear rates, the curves, irrespective of the value of ε'_0, go over the LVE prediction when the link tension coefficient is a constant (cf. Fig. 9); this is not substantiated by rheological data [see Fig. 2(a) of Ref. 21].

In Fig. 10, we compare the predictions of the second viscometric function after start-up of shear flow from an isotropic sample. In selecting physically meaningful values of the parameter ε_0, we need to make sure that they do not lead to a change of sign for $\Psi_2(t)$ at small times. To respect this constraint by construction, we have derived an approximate criterion for the largest value of ε_0 that can be employed so that $\Psi_2(t)$ does not exhibit a change of sign (see Sec. C of the supplementary material). For this reason, the values of ε_0 in Fig. 10 are different from those of Figs. 6 and 9, where we explored a wider ε_0 range. We find that the predictions under
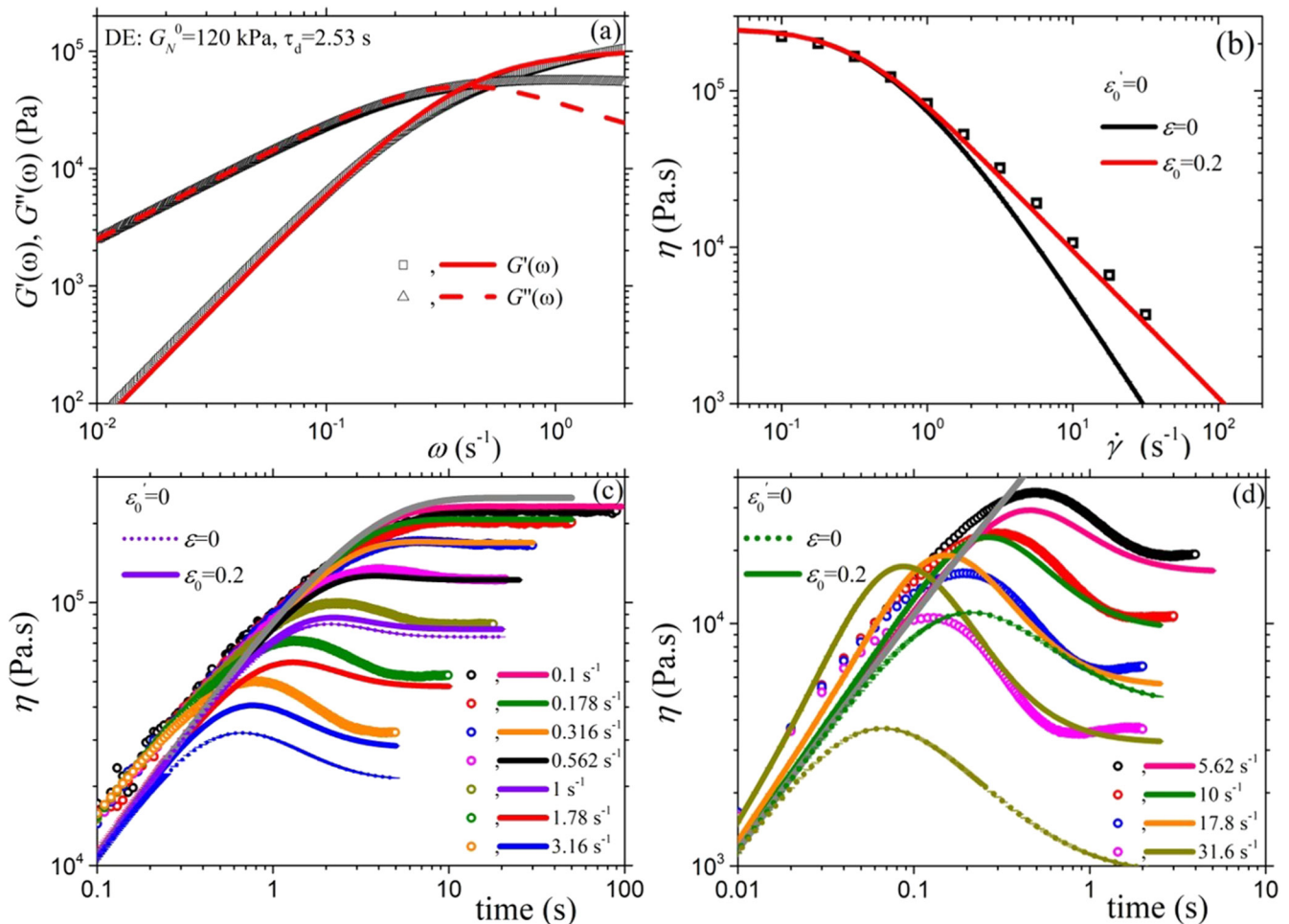

FIG. 11. Comparison of experimental data for the polymer melt PS185k by Costanzo *et al.*[28] at 160 °C (symbols) with the tumbling-snake model predictions (lines) for the storage and loss moduli (a), the steady-state shear viscosity (b) (along with the predictions of the DE model, $\varepsilon'_0 = \varepsilon = 0$), and the start-up shear viscosity (c) and (d). In (c) and (d), the thick gray line depicts the LVE envelope and different colours have been employed to denote predictions and measurements. In (b)-(d), the short-dotted lines depict the predictions of the DE model (with $\varepsilon = 0$) for 1, 3.16, 10, and 31.6 s^{-1}.

constant ε_0' are practically insensitive to the value of ε_0. This was also the case for the steady-state value presented in Fig. 4. In addition, we observe a slight increase of the curves upon increasing ε_0'. And, contrary to Ψ_1, no undershoot is detected at large shear rates. Finally, it should be stressed that by employing the non-constant $\varepsilon = \varepsilon_0 S_2^2$, we avoid the spurious sign changes of Ψ_2 at early times that are evident when a constant, non-vanishing ε is employed (see Fig. S4 of the supplementary material).

It is worth a remark that the material functions scaled by N-dependent modulus G and relaxation time λ,[21,24,26,27] calculated for constant values of the parameters ε_0' and ε, but with a different number of Kuhn segments, N are found to be basically identical for all $N \geq 10$ (comparison not shown). This trend was also noticed for the steady-state values (see Ref. 27).

V. COMPARISON WITH EXPERIMENTAL DATA

As we illustrated recently,[21] the tumbling-snake model is able to compare well with experimental rheological data when it is supplemented by a non-constant link tension coefficient.

Here, we compare against the experimental data provided by Costanzo et al.[28] for the PS185k polymer melt and the PS285k/2k-65 polymer solution which exhibit the same number of entanglements $Z = 13.9$ (thus, in the following $N = 42$). The corresponding predictions for the storage and loss moduli are independent of the value of the parameter ε_0 (see Sec. B of the supplementary material of Ref. 21).

At first, we compare against the storage and loss moduli and the steady-state and transient shear viscosities for the PS185k polymer melt, depicted in Fig. 11. Since the transient viscosity curves do not exhibit a damping behavior, we should take $\varepsilon' = 0$;[21] the corresponding predictions for the storage and loss moduli are therefore those of the DE model. The values $G = 600$ kPa and $\lambda = 25$ s (or $G_N^0 = G/5 = 120$ kPa, $\tau_d = \lambda/\pi^2 = 2.53$ s) compare favorably with the storage and loss moduli [Fig. 11(a)], whereas using $\varepsilon_0 = 0.2$ provides a very good prediction for the steady-state shear viscosity [Fig. 11(b), where the predictions of the DE model are also presented]. The selected values for $G = 600$ kPa and $\lambda = 25$ s predict a zero-shear-rate viscosity equal to $\eta_0 = G\lambda/60 = 2.5 \times 10^5$ Pa s, which is basically identical with the one reported experimentally ($\eta_0 = 2.48 \times 10^5$ Pa s).[28]
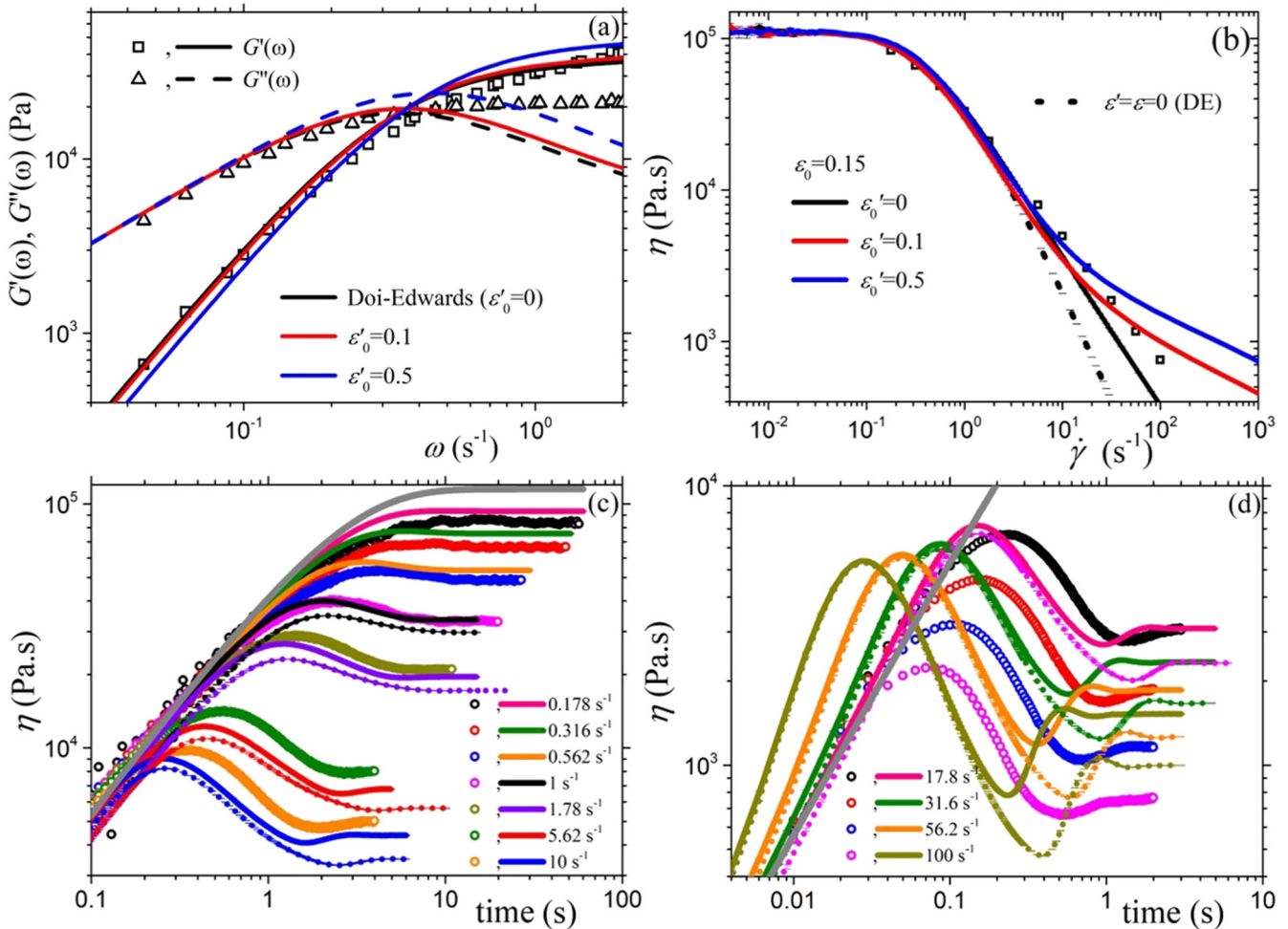

FIG. 12. Comparison of experimental data for the polymer solution PS285k/2k-65 by Costanzo et al.[28] at 150 °C (symbols) with the tumbling-snake model predictions (lines) for the storage and loss moduli (a), the steady-state shear viscosity (b), and the start-up shear viscosity for shear rates (c) and (d); in (c) and (d), the thick gray line depicts the LVE envelope and different colours have been employed to denote predictions and measurements. In (b)-(d), the short-dotted lines depict the predictions with $\varepsilon_0' = 0.1$ for $\dot{\gamma} \geq 1 \text{ s}^{-1}$.
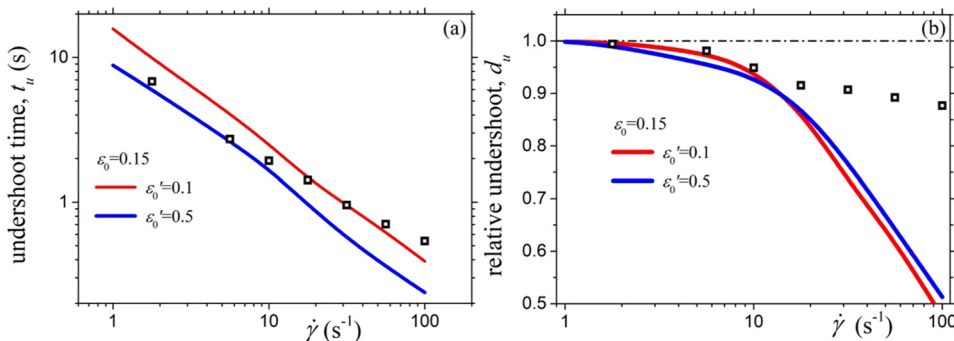
FIG. 13. Same as Fig. 12 but for (a) the undershoot time, t_u, and (b) the relative undershoot depth d_u. Same parameter values as in Fig. 12.

All parameters have thus been chosen, and the discriminating task is to compare against the transient shear viscosity measurements. This is illustrated in Fig. 11(c) for shear rates below $5\,\mathrm{s}^{-1}$ and in Fig. 11(d) for shear rates above $5\,\mathrm{s}^{-1}$. The predictions are seen to be quite favorable for almost all shear rates although the overshoot is missed at large shear rates.

We next compare against the PS285k/2k-65 polymer solution by the same authors, depicted in Figs. 12 and 13. We choose the values $G = 220$ kPa and $\lambda = 30$ s by comparing with the storage and loss moduli [Fig. 11(a), where a comparison with the DE model is also shown]. The modulus is equal to that given from the expression $G(\phi) = G(1)\phi^{1+\alpha}$, where $G(\phi)$ and $G(1)$ (=600 kPa) are the modulus of the polymer solution and polymer melt, respectively, using a value for the dilution exponent equal to $\alpha = 4/3$. The computed $\eta_0 = 110$ kPa s is very close to the experimental value (104 kPa s[28]). Finally, for the two remaining parameters, we make the choice to depict the predictions for $\varepsilon'_0 = 0.1$ and 0.5, whilst keeping $\varepsilon_0 = 0.15$, as can be seen from the comparison with the steady-state data [Fig. 12(b)]. From the same data, we also see that a better comparison could be obtained if ε'_0 were to be a decreasing function of shear rate, a proposition not new as it was first proposed by Bird *et al.*[26] Such a conclusion is also reached from the transient shear viscosity data [Figs. 12(c) and 12(d)] with primary interest in the undershoot. The value $\varepsilon'_0 = 0.5$ is able to reproduce accurately the experimental measurements at small shear rates, below approximately $20\,\mathrm{s}^{-1}$, whereas the value $\varepsilon'_0 = 0.1$ seems more appropriate at larger shear rates [see Figs. 12(c), 12(d), and 13]. This discrepancy could possibly be amended by considering convective constraint release (CCR) effects,[41–45] which would be quite severe at large shear rates. Another possible reason for the deviation at large shear rates may be the omission in our present treatment of flow-induced alignment of chain ends which are particularly important in the case of shear viscosity.[32,37]

Overall, the tumbling-snake model with a link tension coefficient given by $\varepsilon = \varepsilon_0 S_2^2$ appears able to capture the LVE behavior and the steady-state and transient behavior of the shear viscosity for entangled polymer melts (Fig. 11). The same holds true for concentrated polymer solutions as well (Figs. 12 and 13), but at larger shear rates (after about $20\,\mathrm{s}^{-1}$ for PS285k/2k-65), it fails to provide a good fitting, which may be due to the omission of important mechanisms particularly relevant at large shear rates, as mentioned above.

VI. CONCLUSIONS

In this work, we provided and discussed the solution of the Curtiss-Bird model for concentrated solutions and entangled polymer melts (the tumbling-snake model) subjected to both steady-state shear flow and start-up shear flow. We first discussed the predictions of the tumbling-snake model and the reasons for employing a non-constant link tension coefficient in Ref. 21. In the present work, we provided a very thorough parametrization of the predictions of the model. We illustrated that the use of a constant link tension coefficient is not in line with various experimental data,[21,28,31] as the model then predicts that the shear viscosity approaches the constant value $\varepsilon/90$ as $t \to 0$ and that Ψ_2 spuriously changes sign in the course of time (See Sec. B of the supplementary material). The use of a time- and Wi-dependent link tension coefficient completely fixes both of these unnatural predictions.

Overall, we feel that the tumbling-snake model has shown the necessary capacity to compare well with experimental data and should be considered as a possible framework for further refinement in the future. We plan accounting for contour length fluctuations (CLFs),[4,5] that have been neglected in the treatment of CB (and of the original work of DE). One way to account for CLF is by considering a σ-dependent curvilinear segment diffusion along the polymer's contour (see e.g. Refs. 14–16 and references therein), which is expected to improve the comparison of the storage and loss moduli with rheological data at intermediate frequencies. Also, the consideration of CCR effects[41–45] is today known to affect quite significantly the rheological properties at intermediate and large shear rates. Finally, and as alluded to in Sec. II, we should elaborate further as to how flow-induced alignment of chain ends[32,37] affects the boundary conditions for the single-link distribution function [cf. Eq. (2)]. Given the capacity of the tumbling-snake model, defended in this work and in Ref. 21, to compare rather well with available rheological data, particularly for polymer melts, its further refinement is expected to improve it even more and therefore, in time, elevate its constitutive maturity to that of the tube model.

SUPPLEMENTARY MATERIAL

See supplementary material for additional analytical predictions of the tumbling-snake model and BD predictions for the transient material functions of the tumbling-snake model

when a constant link tension parameter is employed, and the derivation of a criterion that helps avoiding a sign change in the transient second normal stress coefficient.

ACKNOWLEDGMENTS

[1] M. Doi and S. F. Edwards, J. Chem. Soc., Faraday Trans. 2 **74**, 1789 (1978).

[2] M. Doi and S. F. Edwards, *The Theory of Polymer Dynamics* (Clarendon, Oxford, 1986).

[3] P. G. de Gennes, J. Chem. Phys. **55**, 572 (1971).

[4] H. Watanabe, Prog. Polym. Sci. **24**, 1253 (1999).

[5] T. C. B. McLeish, Adv. Phys. **51**, 1379 (2002).

[6] M. Kröger, Comput. Phys. Commun. **168**, 209 (2005).

[7] K. N. Foteinopoulou, N. C. Karayiannis, V. G. Mavrantzas, and M. Kröger, Macromolecules **39**, 4207 (2006).

[8] C. Tzoumanekas and D. N. Theodorou, Macromolecules **39**, 4592 (2006).

[9] S. H. Jeong, J. M. Kim, J. Yoon, C. Tzoumanekas, M. Kröger, and C. Baig, Soft Matter **12**, 3770 (2016).

[10] P. S. Stephanou, C. Baig, G. Tsolou, V. G. Mavrantzas, and M. Kröger, J. Chem. Phys. **132**, 124904 (2010).

[11] C. Baig and V. G. Mavrantzas, Soft Matter **6**, 4603 (2010).

[12] C. Baig, P. S. Stephanou, G. Tsolou, V. G. Mavrantzas, and M. Kröger, Macromolecules **43**, 8239 (2010).

[13] J. Qin, S. T. Milner, P. S. Stephanou, and V. G. Mavrantzas, J. Rheol. **56**, 707 (2012).

[14] P. S. Stephanou, C. Baig, and V. G. Mavrantzas, Macromol. Theory Simul. **20**, 752 (2011).

[15] P. S. Stephanou, C. Baig, and V. G. Mavrantzas, Soft Matter **7**, 380 (2011).

[16] P. S. Stephanou and V. G. Mavrantzas, J. Non-Newtonian Fluid Mech. **200**, 111 (2013).

[17] Y. Li, B. C. Abberton, M. Kröger, and W. K. Liu, Polymers **5**, 751 (2013).

[18] K. S. Schweizer and J. G. Curro, Adv. Chem. Phys. **98**, 1 (1997).

[19] Y. Li, S. Tang, M. Kröger, and W. K. Liu, J. Mech. Phys. Solids **88**, 204 (2016).

[20] P. S. Stephanou and V. G. Mavrantzas, J. Chem. Phys. **140**, 214903 (2014).

[21] P. S. Stephanou, T. Schweizer, and M. Kröger, J. Chem. Phys. **146**, 161101 (2017).

[22] C. F. Curtiss and R. B. Bird, J. Chem. Phys. **74**, 2016 (1981).

[23] C. F. Curtiss and R. B. Bird, J. Chem. Phys. **74**, 2026 (1981).

[24] R. B. Bird, H. H. Saab, and C. F. Curtiss, J. Chem. Phys. **77**, 4747 (1982).

[25] R. B. Bird, H. H. Saab, and C. F. Curtiss, J. Phys. Chem. **86**, 1102 (1982).

[26] R. B. Bird, R. C. Armstrong, and O. Hassager, *Dynamics of Polymeric Liquids: Volume 2, Kinetic Theory* (John Wiley & Sons, New York, 1987).

[27] P. S. Stephanou and M. Kröger, J. Chem. Phys. **144**, 124905 (2016).

[28] S. Costanzo, Q. Huang, G. Ianniruberto, G. Marrucci, O. Hassager, and D. Vlassopoulos, Macromolecules **49**, 3925–3935 (2016).

[29] M. H. N. Sefiddashti, B. J. Edwards, and B. Khomami, J. Rheol. **59**, 119 (2015).

[30] J. M. Kim and C. Baig, Sci. Rep. **6**, 19127 (2016).

[31] D. Auhl, J. Ramirez, A. E. Likhtman, P. Chambon, and C. Fernyhough, J. Rheol. **52**, 801 (2008).

[32] M. Kröger, *Models for Polymeric and Anisotropic Liquids* (Springer, New York, 2005), Vol. 675.

[33] R. S. Graham, A. E. Likhtman, T. C. B. McLeish, and S. T. Milner, J. Rheol. **47**, 1171 (2003).

[34] M. Fang, M. Kröger, and H. C. Öttinger, J. Rheol. **44**, 1293 (2000).

[35] J. D. Schieber, D. M. Nair, and T. Kitkrailard, J. Rheol. **51**, 1111 (2007).

[36] H. C. Öttinger, *Stochastic Processes in Polymeric Fluids: Tools and Examples for Developing Simulation Algorithms* (Springer, Berlin, 1996).

[37] M. Kröger and S. Hess, Phys. A **195**, 336 (1993).

[38] R. B. Bird, H. R. Warner, and D. C. Evans, Adv. Polym. Sci. **8**, 1 (1971), https://link.springer.com/chapter/10.1007/3-540-05483-9_9.

[39] B. Huber, M. Harasim, B. Wunderlich, M. Kröger, and A. R. Bausch, ACS Macro Lett. **3**, 136 (2014).

[40] M. B. Harasim, B. Wunderlich, O. Peleg, M. Kröger, and A. R. Bausch, Phys. Rev. Lett. **110**, 108302 (2013).

[41] G. Marrucci, J. Non-Newtonian Fluid Mech. **62**, 279 (1996).

[42] G. Ianniruberto and G. Marrucci, J. Non-Newtonian Fluid Mech. **65**, 241 (1996).

[43] G. Marrucci and G. Ianniruberto, Philos. Trans. R. Soc., A **361**, 677 (2003).

[44] P. S. Stephanou, I. C. Tsimouri, and V. G. Mavrantzas, Macromolecules **31**, 3161 (2016).

[45] H. C. Öttinger, J. Non-Newtonian Fluid Mech. **89**, 165 (2000).